

31 **Introduction**

32 Louisiana has approximately 160 movable bridges, mostly in the southern part of the state.
33 This places Louisiana among the states with the highest inventory of movable bridges in the nation.
34 These transportation arteries are important for the economic well-being of the state, as well as for
35 the safety of the inhabitants in hurricane vulnerable regions during evacuations. Most of the
36 movable bridges in Louisiana are either swing-span or lift-bridge type structures. Very few
37 movable steel bridges are of the bascule type.

38 The typical deck systems in movable bridges are open steel grids, which typically consist of
39 either diagonal or rectangular grids (Fig. 1). The diagonal grids were first used in the 1920s and
40 represent the oldest lightweight deck system (Gase 2008). The traditional steel grid decks are
41 supported by steel stringers at typically 1.22 m on center. On average these decks weigh less than
42 1.20 kN/m^2 ; while some others can weigh as little as 0.67 kN/m^2 (Mirmiran et al. 2009). This deck
43 system is attractive because it is light weight, the panels are prefabricated and they are easy to
44 install and replace. Also, deck crowning, scuppers, and drains are not required, since rain water
45 drains through the openings in the deck (Mirmiran et al. 2009). Additionally, the light weight helps
46 with imposing as little of a demand as possible on the mechanical system. However, records show
47 that steel grids have exhibited durability issues. The proximity of these exposed steel systems to
48 humid environments leads to rapid deterioration. As a result, decks become loose, causing extreme
49 noise. Furthermore, inhabitants in areas close to movable bridges often complain about noise levels
50 resulting from vehicles crossing over the steel grids. These problems are aggravated by trapping
51 foreign debris throughout the deck grids. The lack of traction in steel grid decks is another concern
52 with respect to safety.

53 The Louisiana Department of Transportation and Development (LADOTD) has an interest in
54 using concrete decks to replace deteriorated steel grids on existing movable bridges as well as in
55 new construction. However, the mechanical systems of moveable bridges are highly sensitive. As
56 a result, any decking used to replace or rehabilitate the existing steel grid decking should match
57 the weight of the existing steel grid such that the mechanical system operates as designed. The
58 weight to strength ratio of conventional concrete decks will have a negative impact on the load
59 demand imposed on the mechanical system. Accordingly, a light ultra-high/high performance
60 concrete (UHPC/HPC) deck is proposed as an alternative to steel grid decking. The current
61 definition of UHPC under review in the technical committee of the American Concrete Institute
62 (ACI 239) (2015) is: “Concrete that has a minimum specified compressive strength of 150 MPa
63 with specified durability, tensile ductility and toughness requirements; fibers are generally
64 included to achieve specified requirements”. High-performance concrete is defined as concrete
65 meeting special combinations of performance and uniformity requirements that cannot always be
66 achieved routinely using conventional constituents and normal mixing, placing, and curing
67 practices (ACI CT 2013). The UHPC/HPC deck system is intended to provide a continuous driving
68 surface that mimics monolithic construction, provides integral connections with the supporting
69 stringers as well as between adjacent deck panels, and provides traction, which should improve
70 traffic safety.

71 Florida Department of Transportation (FDOT) in collaboration with URS Corporation
72 identified several potential alternative lightweight solid deck systems to replace steel open grid
73 decks on typical Florida bascule bridges (Mirmiran et al. 2009; 2012; Phillips 2014; and Mirmiran
74 and Ghasemi 2016). These deck systems include a sandwich plate system, a fiber reinforced
75 polymer (FRP) composite deck, an aluminum orthotropic deck, a prismatic concrete deck with

76 FRP tubes, a non-prismatic concrete deck with FRP tubes, a FRP deck, and a waffle slab UHPC
77 deck. The sandwich plate system and the FRP composite systems are vulnerable to delamination,
78 debonding and cracking of wearing surface. The aluminum orthotropic deck is a patented product,
79 and requires expansion joints, periodic replacement of the wearing surface, galvanic corrosion
80 mitigation, as well as the potential use of blind-type fasteners (Mirmiran et al. 2009). The UHPC
81 deck with FRP tubes was not investigated with respect to the performance of panel to stringer
82 connections, panel to panel connections, and fatigue performance of the system. The deflection of
83 the FRP deck system under service load significantly exceeded the deflection limit suggested by
84 the American Association of State and Transportation Officials (AASHTO) Load and Resistance
85 Factor Design (LFRD) Specifications (2014) (Article 9.5.2). The stiffness of the FRP deck was
86 enhanced by adding an UHPC layer on the top. The dominant mode of failure in the FRP deck
87 with an UHPC overlay was either at the interface of FRP and UHPC, or through buckling of the
88 FRP web.

89 The UHPC waffle slab system was investigated further by Mirmiran et al. (2012) and Mirmiran
90 and Ghasemi (2016). Both MMFX₂ bars and carbon fiber reinforced polymer (CFRP) bars were
91 investigated as reinforcement alternatives for the waffle slab configuration. The overall thickness
92 of the waffle slab configuration varied from 102 mm to 127 mm, and the spacing between the
93 stringers was 1.22 m. The weight limitation was 1.01 kN/m². The waffle slab configuration proved
94 to be a viable alternative to steel grid decks for Florida's movable bridges by meeting AASHTO's
95 (2014) load demands.

96 As it will be described in the next section there are some differences between the characteristics
97 of the steel grid decks in Florida compared to those in Louisiana. The predominant depth of the
98 existing steel grids in Louisiana is 132 mm compared to the 102-127 mm range investigated in

99 Florida. The maximum weight limitation for Louisiana's movable bridge decks is 0.96 kN/m^2
100 compared to the 1.01 kN/m^2 weight limit for Florida's bascule bridge decks. The majority of
101 movable bridges in Louisiana featured steel grid spans, defined as the distance between the
102 centerlines of stringers, less than or equal to 1.27 m compared to 1.22 m in Florida. At first glance
103 these differences may appear small or negligible taking into the consideration the accuracy
104 typically employed in structural engineering work. However, given the strict limitation on the
105 maximum weight imposed on the mechanical system, such small differences required the
106 development of a unique deck configuration for Louisiana's movable bridges. The UHPC deck
107 configuration developed in Florida, while viable for Florida's bascule bridges could not be directly
108 applied to Louisiana's movable bridges for the following reasons: 1) the maximum weight limit is
109 greater than that determined for Louisiana's bridges, 2) the depth of the deck was shallower than
110 the predominant depth recorded for Louisiana's bridges, thereby increasing the overall depth
111 would further exceed the maximum weight limit, 3) the span between the centerlines of stringers
112 is 51 mm shorter than that determined for Louisiana's bridges.

113 Aaleti et al. (2011; 2013) developed an UHPC waffle slab for non-movable bridges. There was
114 no limitation on the maximum weight of the deck. The overall depth of the slab was 203 mm. The
115 thickness of the flange was 64 mm and the thickness of the transverse ribs varied from 76 mm at
116 the bottom to 102 mm at the top. The range of spans considered varied from 1.22 m to 3.05 m. The
117 weight of this deck system far exceeds the maximum weight limitation for Louisiana's movable
118 bridges (0.96 kN/m^2) because the deck configuration was developed for non-movable bridges.
119 However, the female-to-female type panel to panel connections provided a good starting point and
120 are similar to the detail proposed for Louisiana movable bridges.

121 The goal of this research is to develop an UHPC/HPC deck system for Louisiana's movable

122 bridges. A modified version of the waffle slab UHPC deck investigated in Florida is proposed for
123 investigation in this study because: 1) it can meet the limitations on weight and overall depth for
124 Louisiana's movable bridges, 2) it can meet load and deflections demands specified in AASHTO
125 (2014), 3) it uses high strength corrosion resistant reinforcement, 4) it uses panel to panel and
126 panel to stringer connections that are intended to emulate monolithic action, and 5) it includes
127 either a chip seal surface coating or a controlled broom finish to provide skid resistance and
128 increase traction.

129 **Compilation of Louisiana's current moveable bridge deck system details**

130 A list of movable bridges that utilize steel grid decking was obtained from LADOTD. The
131 bridge plans including as-built drawings and shop drawings were searched to collect all relevant
132 information such as: panel thickness, panel weight, panel length, cantilever length, span length,
133 and stringer size. Cantilever length was defined as the distance from the centerline of the exterior
134 stringer to the edge of the steel grid. Span length was defined as the distance between the
135 centerlines of stringers. The bridge plans for a total of 17 bridges were investigated during the
136 period of time allocated to complete this task. The minimum and maximum deck thickness were
137 129 mm and 150 mm, respectively. The predominant deck thickness was 132 mm. There was a
138 minimum deck weight requirement only for two bridges (0.77 kN/m^2 and 0.84 kN/m^2). The
139 maximum deck weight limitation based on stringer reactions was typically 0.96 kN/m^2 with the
140 exception of one bridge for which this limitation was 0.86 kN/m^2 . The most common stringer type
141 was W410×54. The spacing of stringers varied from 1.12 m to 1.42 m, however the majority of
142 bridges featured stringer spacing less than or equal to 1.27 m.

143 Based on the collected information the following recommendations were made with the respect
144 to the development of UHPC deck panels (Table 1). The panel thickness is recommended to be

145 132 mm to be consistent with the predominant existing grid deck thicknesses. The maximum panel
146 weight should be limited to 0.96 kN/m^2 so that specified maximum stringer reactions are not
147 exceeded. The span length should be 1.27 m to cover the majority of the investigated bridges. The
148 panel length should be such that it covers at least three spans to take advantage of continuity and
149 reduce the number of joints exposed to traffic. Alternatively, continuity for superimposed loads in
150 the transverse direction can be achieved by placing a site cast UHPC/HPC diaphragm between the
151 ends of the individual precast waffle slab deck panels. This detail is illustrated in the next section.
152 The stringer size that should be considered during the development of the UHPC deck is W410×54
153 because this was the most common size.

154 **Proposed Precast Deck System**

155 The proposed system is illustrated in Fig. 2, 3 and 4. Two deck configurations are investigated
156 with respect to the number of longitudinal ribs. These two deck configurations (denoted as Deck
157 System 1 and Deck System 2 in Fig.2a) were determined based on preliminary work performed by
158 Menkulasi et al. (2016). In the first configuration there is only one partial depth longitudinal rib at
159 mid-span of the panel, which helps distribute loads to the adjacent ribs. The dimensions of this
160 partial depth rib are 22 mm wide and 70 mm deep from the bottom of the top flange. In the second
161 configuration there are a total of six partial depth longitudinal ribs. The width of these ribs is 22
162 mm whereas the depth is 19 mm. Both panel configurations will receive a chip seal surface coating
163 or a controlled broom finish to provide traction. The weight of the chip seal surface coating is
164 negligible.

165 Continuity for live loads in the transverse direction is achieved by placing a cast-in-place (CIP)
166 UHPC/HPC diaphragm between the ends of the precast deck panels when they are fabricated as
167 single span panels (Fig. 2a and Details C1a and C2a in Fig. 3 and Fig. 4). There is a distance of 24

168 mm between the end of the panels and the centerline of the stringers to allow for the placement of
169 the cast-in-place UHPC/HPC diaphragm. The top flange at the ends each panel is coped 76 mm in
170 length and 11 mm in depth to allow the C-grid to project past the ends of the panels, be immediately
171 above the coped flange and lap with the C-grid from the adjacent panels. The C-grid projects 76
172 mm past the ends of the panel to create a 152 mm lap with the grid coming for the adjacent panel
173 (Details C1a and C2a in Fig. 3 and Fig.4). All the interfaces between precast and cast-in-place
174 UHPC/HPC in the proposed connections should be sandblasted and kept moist at surface saturated
175 dry conditions to enhance bond.

176 When deck panels are fabricated such that they cover two or more spans the details will be
177 similar with the exception that the flange and transverse ribs will be continuous over the supports
178 and the cast-in-place concrete diaphragm will be placed through access holes from the top of the
179 precast deck (Fig. 2b and Details C1b and C2b in Fig. 3 and Fig. 4).

180 Continuity in the direction of traffic is provided by using female-to-female type panel to panel
181 connections and a cast-in-place UHPC/HPC fill (Details B1 and B2 in Fig. 3 and Fig.4). The steel
182 stringers are spaced at 1.27 m on center. The width of a single precast panel is 1.22 m. The overall
183 depth of the deck panels is 132 mm. The thickness of the flange is 22 mm. The width of the
184 transverse ribs, which will act as T-beams to support the superimposed loads varies; it is 51 mm
185 at the bottom of the stem and it tapers down to 22 mm (Details A1 and A2 in Fig. 3 and Fig. 4).
186 The width of end ribs at the bottom is equal to 38 mm for deck configuration 1 and 32 mm for
187 deck configuration 2.

188 The spacing of the transverse ribs is 406 mm center to center for the interior ribs and 406 mm
189 from the center of the interior rib to the outside face of the exterior rib. The weight of a single
190 panel considering the cast in place UHPC/HPC diaphragm is 0.964 kN/m^2 for deck system 1 and

191 0.955 kN/m² for deck system 2. The weight of deck system 1 is slightly over the target weight of
192 0.96 kN/m² and was calculated using a measured unit weight of 2500 kg/m³ for *Ductal*. *Ductal* is
193 a commercial UHPC/HPC formulation provided by Lafarge North America and was supplied to
194 the research team by Lafarge as part of this study. The panel weight was calculated by ignoring
195 the presence of the reinforcement bars and mesh because the unit weight of reinforcement was less
196 than that of concrete.

197 Glass fiber reinforced polymer (GFRP) bars (GFRP V-ROD HM - 60GPa Grade III) are
198 proposed as positive moment reinforcement in the transverse and longitudinal ribs. GFRP bars are
199 corrosion resistant and are produced by Pultrall Inc. Each interior transverse rib is reinforced with
200 a No. 16 GFRP bar at the bottom and each exterior rib is reinforced with a No. 13 GFRP bar. The
201 partial depth longitudinal ribs in both configurations are reinforced with a No. 10 GFRP bar to
202 help distribute wheel loads in the longitudinal direction. The clear bottom cover to positive
203 moment reinforcement is 11 mm in the interior ribs and 10 mm in the exterior ribs. The clear cover
204 in all other cases is equal to 6 mm or greater.

205 Flange reinforcement consists of a two-way non-corrosive carbon fiber grid (C-grid)
206 developed by Chomarat North America. C-grid is an epoxy-coated composite grid made with
207 cross-laid and superimposed carbon fiber. The diameter of the strands in the C-grid is 2 mm and
208 the spacing of the strands is 41 mm in the longitudinal direction and 46 mm in the transverse
209 direction (C50 –46 x 41).

210 **Finite Element Analysis**

211 ***Introduction and Validation***

212 Several nonlinear finite element analyses were performed to investigate the behavior of the
213 proposed deck panels from the onset of loading to failure. The commercially available finite

214 element analysis software Abaqus was used in all numerical simulations. The finite element
215 models were validated based on laboratory tests performed in Florida for the deck system
216 developed by Mirmiran et al. (2009). The results from the finite elements models were compared
217 with Florida's test results in terms of load displacement curves, peak loads, and crack patterns at
218 failure. Four different simulations were performed: 1) a typical T-section in a single span condition
219 (1T1S), 2) a typical T-section in a two-span continuous condition (1T2S), 3) a simply supported
220 panel that featured four spaces between the ribs (4T1S), and 4) a two span continuous panel that
221 featured three spaces between the ribs (3T2S). Single symmetry and double symmetry were
222 utilized as much as possible during the numerical simulations to reduce analysis time. Fig. 5 shows
223 the finite element mesh, boundary conditions and the double symmetry used during the simulation
224 of the 1T1S specimen.

225 3D continuum elements were used in all simulations. The size of the mesh was selected
226 such that each element side did not exceed 13 mm in length and was determined based on results
227 from convergence studies to provide a balance between accuracy and computational expense. The
228 nonlinear behavior of concrete was simulated using the concrete damage plasticity approach
229 available in Abaqus developed by Lubliner et al. (1988) and Lee and Fenves (1998). The uniaxial
230 behavior of concrete in compression and tension as well as that for the MMFX₂ bars was based on
231 the data reported by Mirmiran et al. (2009) and is provided in Fig. 6. The uniaxial tensile stress of
232 concrete past tensile strains of 0.01 was maintained at 1 MPa to avoid convergence issues. Table
233 2 provides the parameters used in the concrete damage plasticity model. These parameters were
234 based on calibration as well as on recommendations from Abaqus documentation (2016) and Malm
235 et al. (2006). Dilation angle represents concrete's internal friction angle. Malm et al. (2006)

236 showed that low values of dilation angle correspond to brittle behavior, while higher values
237 correspond to ductile behavior. The value of dilation angle used in this study is 45°.

238 The value of eccentricity is related to the ratio between the tensile strength and compressive
239 strength of concrete and typically is taken equal to 0.1. Therefore an eccentricity value of 0.1 was
240 adopted in this study. $\sigma_{b0} / \sigma_{c0}$ is the ratio of initial equibiaxial compressive yield stress to the initial
241 uniaxial compressive yield stress. This value was assumed to be 1.77 based on the work performed
242 by Sercombe et al. (1998). K is the ratio of the second stress invariant on the tensile meridian to
243 that on the compressive meridian at initial yield for any given value of the pressure invariant such
244 that the maximum principal stress is negative (Abaqus 2016). This ratio varies from 0.5 to 1.0 and
245 a typical assumed value in the concrete damaged plasticity approach is 0.67. Therefore K was
246 taken equal to 0.67. The viscosity parameter was assumed to be zero in this study.

247 Fig. 7 compares the experimental and numerical load versus mid-span displacement curves
248 for all four specimens. The numerically obtained load versus mid-span displacement curves for
249 specimens 1T1S, 4T1S, and 3T2S compare rather well with the experimentally obtained curves,
250 featuring only minor differences during the entire loading. The experimental and numerical curves
251 for 1T1S and 4T1S are almost identical. For the 1T2S specimen the curves are different up until a
252 displacement of 13 mm. After that the curves become very similar. It should be noted that both
253 numerical and experimental models showed an increase in stiffness for the two-span continuous
254 configurations compared to the single span configurations with the exception of tested specimen
255 1T2S, which did not show this expected trend. Considering the test setup, one possible explanation
256 for the differences between experimental and numerical load displacement curves for specimen
257 1T2S could be a delayed proper sitting of either the loading plate on the specimen or the specimen
258 on the supports.

259 Table 3 shows a comparison of peak loads obtained analytically and experimentally. The
260 average of the ratios between the numerically obtained peak load and that obtained experimentally
261 is 1.00 and the coefficient of variation is 6%. In all four cases the ratios vary from 0.92 to 1.05,
262 which indicates that the numerical models predict fairly well the capacity of the panels. Such small
263 differences in terms of peak loads suggest that the numerical model can estimate the capacity of
264 the precast panels with good accuracy. Additionally, a comparison between the numerically
265 obtained principal plastic tensile strains (PE) and crack patterns observed experimentally at failure
266 was performed for all four considered specimens. In this study the principal plastic strain contours
267 are used to qualitatively illustrate the induced damage due to crack formation and propagation
268 rather than provide an accurate depiction of crack patterns such as crack width, length, spacing,
269 etc. Such an endeavor was outside the scope of this paper. The results are shown in Fig. 8. The
270 plastic principal tensile strain contours suggest that the general location of the diagonal tension
271 crack (shear crack) in the web of the 1T1S specimen was simulated fairly well in the numerical
272 model. Additionally, two of the flexural cracks below the longitudinal rib marked in black in the
273 tested specimen match those illustrated by the principal plastic strain contours at the same location
274 in the numerical model. A diagonal shear crack was also observed during the testing of specimen
275 1T2S, and this was replicated in the numerical model near the intermediate support. In both
276 specimens 1T1S and 1T2S the failure mode was one-way shear, whereas specimens 4T1S and
277 3T2S exhibited a combination of punching shear and yield line failure. Fig. 8 shows how the
278 outline of the major crack on the top of the precast panels 4T1S and 3T2S was captured in the
279 numerical simulations.

280 The similarity in terms of load displacement curves, peak loads, and crack patterns at
281 failure suggests that the numerical models can simulate fairly well the behavior of the precast deck

282 panel under monotonic loads. This modeling protocol was used in the development of the movable
283 bridge deck panels for the state of Louisiana. The next section provides a comparison between the
284 two proposed deck configurations in terms of load versus mid-span displacements.

285

286 *Comparison of deck configurations 1 and 2*

287 The two proposed deck configurations were loaded to failure and their performance was
288 compared in terms of the applied load versus mid-span displacement. The investigations featured
289 a single span deck panel simply supported at the steel stringers (Fig. 9). The edges of the panels
290 were assumed to be free. This approach was taken to examine the relative performance of the two
291 deck configurations under service level and ultimate level loads in a simple setup before studying
292 the benefits of continuity and redundancy.

293 *Ductal* was used as the concrete material in both deck configurations. The uniaxial
294 behavior of *Ductal* in compression was characterized by testing in compression cylinders of 51
295 mm diameter and 102 mm height, and by obtaining the full stress-strain relationship. All specimens
296 were moist cured until the day they were tested. Fig. 10 illustrates the uniaxial stress-strain curve
297 used in the nonlinear finite element simulations. The stress-strain curve in compression covers the
298 range from the onset of loading to the peak load. The descending branch in compression was
299 conservatively ignored. The measured modulus of elasticity at 28 days ($E_c = 56,312$ MPa), peak
300 compressive stress ($f_{cm} = 145$ MPa), and the corresponding strain ($\epsilon_{cu} = 0.0026$) are provided in
301 Fig. 10. The measured compressive strength for *Ductal* at 28 days did not quite meet ACI's
302 definition for UHPC (145 MPa versus 150 MPa) but it was only 5 MPa short of doing so.

303 The uniaxial behavior of *Ductal* in tension was characterized by performing splitting
304 tensile strength tests using the approach recommended by Graybeal (2006), who concluded that

305 an adaptation of ASTM C 496 splitting tensile test showed to provide a practical means for
306 determining the tensile cracking strength of UHPC. The splitting tensile strength tests were
307 conducted on cylinders of 102 mm diameter and 203 mm depth by recording the load that caused
308 the first crack and the peak load. The peak load was always higher than the load that caused the
309 first crack. *Ductal* was assumed to exhibit an isotropic behavior up to the formation of the first
310 crack. The measured cracking stress ($f_{tm} = 11.2$ MPa) and peak stress ($f_{tu} = 18$ MPa) at 28 days are
311 provided in Fig. 10 and are similar to the values reported by Graybeal (2006) for untreated
312 specimens at 28 days. The material tested by Graybeal was also the commercial product marketed
313 by Lafarge. The strain corresponding with the peak stress ($\epsilon_{tu} = 0.0065$) as well as the softening
314 modulus ($E_s = 500$ MPa) were based on data from direct tensile tests performed by Park et al.
315 (2012), who recorded both load and displacement to obtain the stress-strain relationship in tension
316 for ultra-high performance hybrid fiber reinforced concrete. The stress-strain curve reported by
317 Park et al. (2012) that most closely matched the first cracking and peak strength measured during
318 this study was used to correlate the peak strength to the corresponding strain. This was done due
319 to the fact that only loads were obtained during the splitting tensile test method. A tensile stress of
320 1 MPa was assumed for tensile strains exceeding 0.01 to avoid convergence issues.

321 The modulus of elasticity for the C-grid was assumed to be 234,430 MPa and was based
322 on literature provided by the manufacturer. The stress-strain relationship for the C-grid was
323 assumed to be linear, and the ultimate strain (ϵ_{fu}) was taken equal to 0.0099.

324 The bond between reinforcement bars and concrete was assumed to be perfect. To validate
325 this assumption the computed maximum stress on the rebars computed from finite element analysis
326 was compared with the developable stress calculated using the guidelines provided in ACI 440.1
327 (2006). The developable stress was calculated using Equation (1).

328
$$f_{fe} = \frac{0.083\sqrt{f'_c}}{\alpha} \left(13.6 \frac{l_e}{d_b} + \frac{c}{d_b} \frac{l_e}{d_b} + 340 \right) \leq f_{fu} \quad (1)$$

329 where

330 f'_c = design concrete compressive strength (145 MPa)

331 α = bar location factor (taken equal to 1.0)

332 l_e = embedment length of reinforcement bar, (635 mm for No. 13, No. 16, No. 19, and
333 No. 22, 330 mm for No. 10).

334 d_b = diameter of reinforcement bar (10 mm for No.10, 13 mm for No.13, and 16 mm for
335 No.16).

336 C = cover to the center of the bar (19 mm for No. 16, 17 mm for No.13, 11 mm for
337 No.10).

338 f_{fu} = design tensile strength of FRP, considering reductions for service environment
339 (1372 MPa for No.10, 1312 MPa for No.13, 1184 MPa for No.16).

340 Embedment length was calculated as the distance from the point of maximum stress in the
341 reinforcement to the end of the reinforcement. Table 4 provides a summary of the maximum
342 computed stress, developable stress and the ratio between the developable stress and maximum
343 computed stress for flexural reinforcement in the longitudinal and transverse directions of the
344 bridge. The ratio between the developable stress and maximum computed stress in the GFRP bars
345 is higher than 1.0 for both transverse and longitudinal bars. These results validate the assumption
346 of a perfect bond between the reinforcement bars and concrete.

347 Both deck configurations were loaded to failure using three different positions for the truck
348 wheel loads namely a_1 , a_2 , and a_3 (Fig. 2). Position a_1 was used to maximize positive bending by
349 locating the center of the tire print at mid-span. Position a_2 was used to maximize one-way shear
350 effects by locating the edge of the tire print at a distance d (113 mm) from the internal face of

351 stringer support. Position a_3 was intended to maximize punching shear effects, by locating the tire
352 print in deck configuration 1 in such a way that the top flange of the deck was the only component
353 providing resistance. In deck configuration 2 the components providing resistance are the top
354 flange and the longitudinal ribs.

355 Fig. 11 shows that the performance of deck configuration 2 under the various load positions
356 is better than that of deck configuration 1. In all cases the peak load obtained for deck configuration
357 2 is higher than both the service level and ultimate level loads. All numerical simulations that do
358 not exhibit a descending branch ended at the last converged load step. Service level load (95 kN)
359 was calculated as the load corresponding to one wheel for an HL-93 truck (71 kN) times the
360 dynamic load allowance (1.33). The ultimate level load (166 kN) was calculated as the service
361 level load times the live load factor of 1.75. The difference between the peak loads obtained for
362 deck configuration 1 and 2 for tire positions a_1 and a_2 varied from 53 kN to 85 kN. For tire position
363 a_3 the difference between the peak loads was 75 kN. Deck configuration 2 exhibited larger
364 deflection capacity compared to deck configuration 1. Such deflection capacity is essential when
365 the deck is subject to ultimate level loads because it provides an opportunity for the adjacent ribs
366 or deck panels to share the load once cracking, yielding or softening takes place at the most critical
367 location. In general, deck configuration 2 was stronger and more ductile but it also softened at
368 lower loads. For example for load position a_1 the stiffness of the deck configuration 2 is noticeably
369 lower than the stiffness of deck configuration 1 even for loads lower than the service level load.
370 Because deck configuration 2 performed much better than deck configuration 1, this configuration
371 was selected for all subsequent analyses.

372 The influence of tire position on the capacity of the deck panel was further examined by
373 investigating three additional loading positions namely b_1 , b_2 , and b_3 on deck configuration 2 (Fig.

374 2). These additional tire positions match with tire positions a_1 , a_2 , and a_3 with respect to their
375 locations from the stringer supports, however the wheel loads in these cases are centered over the
376 ribs rather than in between them. Fig. 12 suggests that the peak loads for load positions a and b
377 were generally similar. The differences in peak loads varied from 13 kN to 22 kN.

378 Fig. 13 illustrates the principal plastic tensile strains at failure for all load positions
379 described so far. The black color represents principal plastic tensile strains that are equal to or
380 greater than 0.0065, which is the strain that corresponds with the peak tensile strength measured
381 during the material characterization study. Load position a_1 featured mid-span loading with the
382 load placed between the transverse ribs. As a result, there is significant cracking in the flange and
383 in the longitudinal ribs immediately underneath the load. Once the load is transferred to the
384 transverse ribs the majority of the cracks take place in the webs of the transverse ribs due to their
385 reduced thickness. Additionally, there are some flexural cracks in the bottom of the transverse ribs
386 at mid-span. The overall behavior of the deck panel for this load position can be characterized as
387 follows: flexural cracking will initiate at the bottom of longitudinal ribs followed by flexural
388 cracking at the bottom of top flange and bottom of stem; formation of shear cracks in the stem will
389 ensue; the ultimate condition is expected to be a shear failure of the stem.

390 For load position a_2 the principal plastic tensile strain contours in the flange are similar to
391 those observed for load position a_1 . However, as expected, the plastic strain contour in the webs
392 of the transverse ribs is more pronounced in the more heavily loaded side of the span. In addition
393 to the shear cracks in the web of the transverse ribs, there are also shear-flexural cracks at the
394 bottom of the transverse ribs, flexural cracks near mid-span, as well as some cracking at the bottom
395 of the transverse ribs near the support. The overall behavior of the deck panel for this load position

396 in terms of the sequence of cracking and the ultimate condition is similar to that described for load
397 position a_1 .

398 For load position a_3 the cracking is concentrated in the top flange as well as in the webs of
399 the transverse ribs. Cracking in the transverse ribs is dominated by shear cracking in the web. The
400 failure mode for this load position is expected to be dominated by shear in the stem with the deck
401 panel exhibiting significant flexural cracking at the bottom of the top flange.

402 The principal plastic tensile strain contours for load position b_1 differ from those for load
403 position a_1 because the majority of the cracks take place in the web of the loaded transverse rib as
404 well as in the bottom of the stem as opposed to the top flange. This is due to the fact that the load
405 is centered over the ribs. As stated earlier, cracking in the webs of the transverse ribs is dominated
406 by shear cracks and takes place due the reduced thickness of the web, while cracking in the bottom
407 of the stem features flexure-shear and flexure cracks. The overall behavior of the deck panel for
408 this load position can be characterized as follows: flexural cracking will initiate at the bottom of
409 stem, followed by the formation of shear cracks in the stem; the ultimate condition is expected to
410 be a shear failure of the stem.

411 The principal plastic tensile strain contours for load position b_2 are characterized mainly
412 by shear cracks in the webs of the most heavily loaded transverse ribs, as well as some flexure-
413 shear cracks and flexure cracks at the bottom of the stem. The cracking in the top flange is not as
414 severe as it is for load position a_2 because the load is applied directly over the transverse ribs. The
415 overall behavior of the deck panel for this load position in terms of the sequence of cracking and
416 the ultimate condition is similar to that described for load position b_1 .

417 Finally, the principal plastic tensile strain contours for load position b_3 suggest shear
418 cracking in the webs of the transverse ribs near the support. The overall behavior of the deck panel

419 for this load position is characterized by the formation of shear cracks in the stem, followed by
420 flexural cracking at the bottom of the stem; the ultimate condition is expected to be a shear failure
421 of the stem. The next section describes the details of a parametric study that was undertaken for
422 deck configuration 2 to investigate the influence of a variety of parameters on the performance of
423 the deck panel.

424 *Parametric study*

425 Given that deck configuration 2 showed promise in providing an alternative solution for
426 Louisiana’s movable bridge decks, the influence of a variety of parameters on the performance of
427 the deck panel was investigated. These parameters were: 1) the addition of CFRP stirrups in the
428 webs of the transverse ribs, 2) the influence of more than one layer of C-grid in the top flange, and
429 3) the influence of the uniaxial behavior of *Ductal* in tension on the behavior of the deck panel in
430 terms of strength and stiffness. The single span deck panel simply supported at stringer locations
431 illustrated in Fig. 9 was used for the parametric study to reduce analysis time.

432 Fig. 14 shows the investigated layout of CFRP shear reinforcement in the transverse ribs.
433 The CFRP shear reinforcement consists of the C-grid used as top flange reinforcement. Loading
434 position b_1 was used to investigate the influence of CFRP shear reinforcement on the behavior of
435 the deck panel. Fig. 15a shows that the influence of CFRP stirrups on the performance of the deck
436 panel is negligible. This suggests that the contribution of the CFRP shear reinforcement to the
437 strength of the deck panel compared to the contribution of concrete is much smaller. *Ductal*’s
438 contribution to the shear strength of the panel is provided in terms of compression struts and
439 tension ties. The area of CFRP shear reinforcement is not large enough to make a marked
440 difference. Accordingly, given the small thickness of the web and the fact that the placement of

441 such shear reinforcement will require additional labor and quality control the addition of this type
442 of shear reinforcement is not recommended.

443 Although all the deck panels investigated so far featured single panels simply supported at
444 the stringer locations, the influence of the C-grid on helping the top flange distribute loads between
445 the transverse ribs was investigated by varying the presence and amount of carbon fiber
446 reinforcement. Three cases were analyzed: 1) no C-grid, 2) one-layer of C-grid, and 3) two layers
447 of C-grid. Tire position a_1 was considered in all cases because it featured a load position between
448 the transverse ribs. Fig. 15b suggests that the C-grid increases slightly the capacity of the deck
449 panel. The difference in peak loads is 6 kips for cases that featured no grid and one layer of grid,
450 and 3 kips for cases that featured one layer of grid and two layers of grid. Additionally, the C-grid
451 serves as negative moment reinforcement in regions of negative moment and also helps in
452 controlling crack widths. It is therefore recommended to include at least one layer of the C-grid as
453 reinforcement in the top flange.

454 Finally, the influence of the uniaxial behavior of *Ductal* in tension on the performance of
455 the deck panel was investigated by examining three different uniaxial tensile behaviors. One of the
456 advantages of UHPC is that it can provide considerable resistance in tension compared to normal
457 strength concrete. However, the behavior of UHPC in tension varies widely and depends on fiber
458 orientation as well as the test method used to characterize this behavior. Fig. 16a illustrates the
459 three uniaxial stress-strain relationships in tension considered for this study. The first is the tensile
460 behavior of *Ductal* used in the study performed by Mirmiran et al. (2009), which is characterized
461 by linear elastic behavior up until the first crack and a slight softening behavior after the first crack.
462 The second is similar to the first except that the cracking stress is higher. The softening modulus
463 for both of these cases was assumed to be 35 MPa and the maximum tensile strain was limited to

464 0.01. The cracking stress for the second tensile behavior was based on the measured value during
465 the splitting tensile tests performed for this study. The third behavior is characterized by linear
466 elastic behavior up until the first crack, a hardening branch between the cracking stress and the
467 peak stress, and a softening branch past the peak tensile strength. As stated earlier the softening
468 modulus for third case was 500 MPa and was based on data collected by Park et al. (2012). The
469 maximum tensile strain for the third case was also limited to 0.01. For tensile strains greater than
470 0.01 a tensile stress of 1 MPa was assumed to avoid convergence issues.

471 Fig. 16b suggests that the uniaxial tensile behavior of *Ductal* affects the overall behavior
472 of the deck panel under the applied load. The higher the cracking stress the higher the capacity of
473 the deck panel. Additionally, the hardening behavior after the first crack leads to a higher capacity
474 for the deck panel. While the difference in peak loads is not significant an improved uniaxial
475 behavior in tension leads to a stiffer and slightly stronger response of the deck panel.

476 ***Effect of Continuity***

477 All the numerical simulations performed so far were done on single span deck panels
478 simply supported at the stringer supports. In reality the deck for the movable bridges will consist
479 of several precast deck panels in both the longitudinal and transverse directions of the bridge. To
480 investigate the influence of continuity on the load capacity of the deck panel a two span continuous
481 single deck panel configuration was investigated (Fig. 17a). Various load positions were
482 investigated with the purpose of selecting the one that leads to the lowest peak load for the two-
483 span continuous configuration. These load positions are illustrated in Fig. 17a and feature two HL-
484 93 truck wheel loads spaced 1.83 m apart. Each load position features wheel loads centered over
485 the transverse ribs. This orientation of wheel loads was previously determined to result in the
486 lowest peak load for the single span precast panels. The first two selected load positions were c_1

487 and c_3 . Load position c_1 was expected to maximize shear stresses at the exterior left support. Load
488 position c_3 was expected to maximize flexural positive stresses and deflections in the left span.
489 Load position c_2 was added to capture a loading case between load position c_1 and c_3 . Load position
490 c_4 was expected to maximize shear stresses at the interior support. Load position c_5 represents a
491 case in which half of the wheel load is supported by one panel and the other half by the adjacent
492 panel. Fig. 17b suggests that load positions c_1 , c_4 , and c_5 do not control, and that the most critical
493 cases are load positions c_2 and c_3 (i.e. when one of the wheel loads is placed near mid-span). Load
494 position c_5 did not control because the transverse joint features two exterior reinforced ribs side by
495 side. The differences in load displacement curves between load position c_2 and c_3 are small enough
496 to suggest that additional load cases that feature tire positions between c_2 and c_3 are not warranted.
497 For each load position a nonlinear finite element analysis was performed to obtain the full load
498 versus mid-span displacement curve. These curves are illustrated in Fig. 17b. The vertical axis
499 represents the ratio between the load applied to the deck panels and the ultimate level load for each
500 case. In some cases only a portion of the two wheel loads could be applied to the two span
501 continuous configuration because the spacing of the wheel loads specified in AASHTO is 1.83 m
502 and the span length for the deck panels is 1.27 m. The load position that led to the lowest peak
503 load was load position c_3 . This load position was used to investigate the efficiency of the C-grid
504 as negative moment reinforcement.

505 The influence of the C-grid as negative moment reinforcement was investigated by varying the
506 presence and amount of the carbon fiber reinforcement in the deck panel for load position c_3 (Fig.
507 18a). The service level load was calculated by multiplying the portion of the wheel loads that fell
508 on the two span continuous configuration by the dynamic load allowance (1.33). The ultimate level
509 load was calculated by multiplying the service level load by 1.75. Fig. 18b illustrates the

510 relationship between the total load versus the displacement at the center of the load in the left span.
511 When no layer of C-grid is provided, the peak load (270 kN) is slightly smaller than the ultimate
512 level load (273 kN). When one layer of C-grid is provided, the peak load is increased to 301 kN,
513 and when two layers are provided the peak load is 319 kN. Fig. 18b suggests that there needs to
514 be at least one layer of C-grid in the top flange to meet the ultimate load demand.

515 The ratio between the peak load (301 kN) obtained for load position c_3 in the two span
516 continuous configuration and the ultimate level load (273 kN) is 1.10. This is similar and actually
517 lower than the ratio between the peak load (187 kN) for load position b_1 in the single deck singly
518 supported configuration and the corresponding ultimate level load (166 kN), which is 1.13. This
519 suggests that the ultimate condition is dominated by shear failure and that continuity in the
520 transverse direction does not help in increasing the load capacity of the deck panels. The inclusion
521 of adjacent panels in the direction of traffic may or may not increase the load capacity of the deck
522 system. This was not evaluated because it was outside the scope of work and because the service
523 level and ultimate level loads were surpassed in all investigated cases. The fact that the mode of
524 failure is primarily a shear failure is illustrated in Fig. 19a, which provides an isometric view of
525 the two span continuous configuration from the bottom and depicts the principal plastic tensile
526 strain contours. Regions in black represent areas in which the principal tensile plastic strain is
527 equal to or greater than 0.0065 and are located primarily in the webs of the transverse ribs.

528 Finally, all load displacement curves shown so far demonstrate that the proposed deck panel
529 configuration possesses significant deflection capacity in the nonlinear range regardless of the load
530 position and continuity. In all investigated cases the maximum recorded deflection was at least 20
531 mm. The softening of the load displacement curve typically occurred at a mid-span deflection of

532 approximately 1 mm. As a result, the proposed deck configuration offers a deflection capacity that
533 is at least 20 times the computed elastic displacement.

534 Fig. 19b illustrates the principal plastic tensile strain contours at failure for the two span
535 continuous configuration for two cases. The first case features no C-grid reinforcement in the top
536 flange (left), and the second features one layer of C-grid in the top flange. Only the strain contours
537 for the left span in Fig. 18a are shown. The black color represents those regions in which the plastic
538 strain is higher than or equal to 0.0065, which is the strain that corresponds with the peak tensile
539 strength recorded during the material characterization study. The principal tensile plastic strain
540 contours corroborate the conclusion drawn earlier that there should be at least one layer of C-grid
541 in the top flange. The extent of damage in terms of crack formation is more pronounced in the case
542 that features no layers of C-grid in the top flange. As a result, the presence of the C-grid in the top
543 flange helps control the extent of cracking in addition to increasing the load capacity of the deck
544 panel.

545 *Deflections*

546 Fig. 20 shows the load versus mid-span displacement for the single span simply supported
547 condition and load position b_1 as well as for the two span continuous configuration and load
548 position c_3 up to and beyond service level loads. Load positions b_1 and c_3 led to maximum
549 deflections at service for the single span and two span continuous configurations, respectively. The
550 dashed vertical line represents the maximum allowable deflection for steel grid decks specified in
551 Article 9.5.2 of AASHTO LFRD Specifications (2014), which was calculated as $L/800$. For the
552 simply supported condition the deflection at service is 5.5 mm, which is greater than the allowable
553 limit (1.6 mm). However, when continuity is introduced the deflection at service becomes 2.2 mm,
554 which is 38% larger than the allowable limit. This suggests that while the introduction of continuity

555 did not result in an increase in terms of load capacity for the panel, it resulted in an increase in
556 stiffness. The No.16 bars in the interior transverse ribs were replaced with No.19 and No.22 bars
557 to study their influence on the stiffness of the deck panels. Additionally, the bars in the exterior
558 transverse ribs were changed to No. 16 for both cases. When a No.19 bar is used, the maximum
559 deflection in the two span continuous configuration is 1.7 mm as opposed to the 1.6 mm allowable.
560 When a No.22 bar is used the maximum deflection is 1.5 mm, which is smaller than the allowable
561 limit. The perfect bond assumption was validated for both new bar sizes and the results are shown
562 in Table 4. These results suggest that simply increasing the size of the bottom bars helps satisfy
563 AASHTO's requirement for deflection. Also, it is expected that the introduction of additional
564 panels, both, in the transverse and longitudinal directions should result in deflections that are even
565 lower than the allowable limit.

566 In the light of this discussion it is recommended that the deck panels be fabricated in at least a
567 two span continuous configuration to increase the stiffness of the system by taking advantage of
568 the inherent continuity in such a configuration. Additionally, it is recommended that No. 22 bars
569 be used to meet AASHTO's deflection limit. Even in cases for which AASHTO's deflection limit
570 may not be critical to the performance of the deck system it is recommended that the deck panels
571 be fabricated in at least a two span continuous configuration to reduce the number of joints exposed
572 to traffic.

573 **Conclusions and Recommendations**

574 The development of a high performance concrete deck for movable bridges in the state of
575 Louisiana was presented. The study was analytical in nature and consisted of several validated
576 nonlinear finite element analyses. The primary challenge in developing this deck system was the
577 limitation on the overall weight of the deck panel.

578 Two deck configurations were investigated. The first deck configuration failed to meet ultimate
579 load demands for those load positions that maximized the effects of one-way shear and punching
580 shear. The second deck configuration performed satisfactorily under all load positions by
581 providing load capacities that surpassed service level and ultimate level loads. This deck
582 configuration was used in all subsequent analyses.

583 *Ductal* produced by Lafarge North America was used as the concrete material. An improved
584 uniaxial behavior of *Ductal* in tension appears to improve the overall behavior of the deck panel
585 under load. GFRP bars are recommended as reinforcement for the bottom of the stem because they
586 are light, corrosion resistant, can be fully developed in the available space, and are able to help
587 develop the computed deck panel capacities. One layer of C-grid is recommended to be used as
588 top flange reinforcement to provide negative moment resistance, control cracking, and distribute
589 loads in the longitudinal direction.

590 The presence of the C-grid as shear reinforcement had a negligible effect on the capacity of
591 the deck panel. Accordingly, while the proposed deck configuration satisfies AASHTO's ultimate
592 load demand without any shear reinforcement, other potential shear reinforcement options will be
593 considered during future research provided that shear was critical for the UHPC/HPC waffle slabs.

594 Continuity in the transverse direction did not result in an increase in deck panel capacity
595 compared to the corresponding ultimate load, but it increased the stiffness of the deck system. This
596 increase in stiffness resulted in lower deflections at service. It is recommended that the deck panels
597 be fabricated in at least a two span continuous configuration to increase the stiffness of the system
598 by taking advantage of the inherent continuity in such a configuration. Additionally, it is
599 recommended that No. 22 bars be used for the interior transverse ribs to meet AASHTO's
600 deflection limit (Article 9.5.2). Even in cases for which AASHTO's deflection limit may not be

601 critical to the performance of the deck system it is recommended that the deck panels be fabricated
602 in at least a two span continuous configuration to reduce the number of joints exposed to traffic.

603 The ultimate condition determined based on the principal plastic tensile strain contours at peak
604 loads was dominated by shear failure in the webs of the transverse ribs, with the deck panel
605 exhibiting flexural cracking at the bottom of the stem and bottom of the top flange. Flexural
606 cracking in the top flange was more pronounced for those load positions which featured wheel
607 loading between the transverse ribs.

608 The analytical investigations presented in this paper were based on several assumptions.
609 Physical testing of single span and multiple span deck panels is scheduled in the near future to
610 validate some of the assumptions made during this analytical study. Additionally, in all cases the
611 loading was monotonic. Physical testing of the deck panels under cyclic loading will be conducted
612 to investigate the effects of fatigue on the performance of the deck panels. Also, additional concrete
613 mixes will be investigated and alternative deck panel configurations will be developed with the
614 purpose of arriving at an option that provides the best balance between performance and economy.

615 **Acknowledgments**

616 This study was sponsored by the Louisiana Transportation Research Center (LTRC). The
617 authors would like to thank the project review committee for their comments and their thorough
618 review of the work performed to date. The authors would also like to thank Lafarge North America
619 for donating *Ductal* to conduct the material characterization study. The opinions expressed herein
620 are those of the authors and do not necessarily reflect the views of the sponsor.

621 **References**

622 Aaleti, S., Petersen, B., Sritharan, S. (2013). *Design Guide for Precast UHPC Waffle Deck*

623 *Panel System, Including Connections* (No. FHWA-HIF-13-032), US Department of
624 Transportation, Federal Highway Administration, Washington D.C.

625 Aaleti, S., Sritharan, S., Bierwagen, D., Wipf, T., (2011). “Structural behavior of waffle
626 bridge deck panels and connections of precast Ultra-High-Performance Concrete:
627 Experimental Evaluation”, *Transportation Research Record, Journal of the Transportation
628 Research Board*, (2251), pp.82-92.

629 AASHTO (American Association of State Highway and Transportation Officials). (2014).
630 *AASHTO LRFD Bridge Design Specifications* 6th Edition. Washington, DC.

631 *Abaqus* [Computer Software]. Dassault Systèmes Americas Corp., Waltham, MA.
632 *Abaqus*. (2016). *User’s Manual Version 6.14-2*. Dassault Systemes Simulia Corp.

633 ACI (American Concrete Institute). (2015). “Ultra-High Performance Concrete”, *ACI 239-15*,
634 Farmington Hills, MI.

635 ACI (American Concrete Institute). (2006). “Guide for the Design and Construction of
636 Structural Concrete Reinforced with FRP Bars”, *ACI 440.1R-06*, Farmington Hills, MI.

637 ACI (American Concrete Institute). (2013). “ACI Concrete Terminology”, *ACI CT-13*,
638 Farmington Hills, MI.

639 ASTM (American Society of Testing Materials). (2010). “Standard test method for splitting tensile
640 strength of cylindrical concrete specimens”, *ASTM C496*, West Conshohocken, PA. C496
641 Chomarat North America, Anderson, SC. [[http://www.chomarat.com/en/category/produits/
642 produits-produits/c-grid/?from=technologie](http://www.chomarat.com/en/category/produits/produits-produits/c-grid/?from=technologie)], (Accessed March 2016).

643 Gase, P.M. (2008). ”Prefabricated Steel Grid Bridge Decks”, [[https://www.dot.state.oh.us/
644 engineering/OTEC/2008%20Presentations/55C.pdf](https://www.dot.state.oh.us/engineering/OTEC/2008%20Presentations/55C.pdf)] (Accessed March 2016)

645 Graybeal, B.A. (2006). “Practical Means for Determination of the Tensile Behavior of Ultra-High

646 Performance Concrete”, *Journal of ASTM International*, Vol. 3, No. 8.

647 Lee, J., Fenves, G. L. (1998). “Plastic-Damage Model for Cyclic Loading of Concrete
648 Structures”, *Journal of Engineering Mechanics*, 124 (8), 892–900.

649 Lubliner, J., Oliver, J., Oller, S., Oñate, E. (1989). “A Plastic-Damage Model for Concrete,”
650 *International Journal of Solids and Structures*, 25 (3), 229–326.

651 Malm, R., James, G., Sundquist, H. (2006). “Monitoring and evaluation of shear crack initiation
652 and propagation in webs of concrete box-girder section”, *International Conference on Bridge
653 Engineering Challenges in the 21st Century*, Hong Kong.

654 Menkulasi, F., Parker, J., Montes, C., Baghi, H., Sandrock, J.P., Gomez, S. (2016).
655 “Development of a Sustainable UHPC Deck for Movable Bridges”, *1st International
656 Interactive Symposium on Ultra-High Performance Concrete*, Des Moines, IA, July 18-20,
657 DOI: 10.21838/uhpc.2016.84.

658 Mirmiran, A., Ghasemi, S. (2016). “Lightweight Solid Decks for Movable Bridges – Phase II”,
659 Final Report, Florida Department of Transportation Research Center, FDOT Contract No.
660 BDV29-977-11, January, Tallahassee, FL.

661 Mirmiran, A., Saleem, M., A., Mackie, K., Xia, J. (2009). “Alternatives to steel grid decks” Draft
662 Final Report, Florida Department of Transportation Research Center, FDOT Contract No.
663 BD015RPWO#22, Tallahassee, FL.

664 Mirmiran, A., Saleem, M., A., Mackie, K., Xia, J. (2012). “Alternatives to steel grid decks –
665 Phase II”, Final Report, Florida Department of Transportation Research Center, FDOT
666 Contract No. BDK80 977-06, Tallahassee, FL.

667 Park, S. H., Kim, D. J., Ryu, G. S., Koh, K. T. (2012). “Tensile behavior of ultra-high

668 performance hybrid fiber reinforced concrete”, *Cement and Concrete Composites*, 34(2), 172-
669 184.

670 Phillips, J. (2014). “Bascule Bridge Lightweight Solid Deck Retrofit Research Project”, Florida
671 Department of Transportation, Project Status Report, Tallahassee, FL.

672 Sercombe, J., Toutlemonde, F., J.U.L.M., F. (1998). “From material behavioral to structural design
673 for concrete in high rate dynamics”, *Computational Modelling of Concrete Structures*,
674 Balkema, Rotterdam, ISBN 90 5410 9467.

675

676 **List of Figures**

677 **Fig. 1** Steel grid decks for movable bridges

678 **Fig. 2** Top view of concrete deck systems (all dimensions in mm)

679 **Fig. 3** Deck system 1 details (all dimensions in mm)

680 **Fig. 4** Deck system 2 details (all dimensions in mm)

681 **Fig. 5** Boundary condition and meshing of the FE model for 1T1S specimen

682 **Fig. 6** Stress-strain relationship for a) UHPC and, b) MMFX₂ used by Mirmiran et al. (2009)

683 **Fig. 7** Comparison of experimental and numerical load displacement curves

684 **Fig. 8** Comparison of experimental crack patterns and simulated principal plastic tensile strains

685 **Fig. 9** Panel configuration used in numerical simulations

686 **Fig. 10** Stress-strain relationship (*Ductal*)

687 **Fig. 11** Simulated performance of the two proposed deck systems under various tire positions, a)
688 position a₁, b) position a₂, c) position a₃

689 **Fig. 12** Load versus mid-span displacement for additional load positions in Deck System 2, a)
690 load placed between the ribs, b) load placed over the ribs

691 **Fig. 13** Principal plastic tensile strains at failure for *Ductal* for various load positions

692 **Fig. 14** Position of the CFRP shear reinforcement

693 **Fig. 15** Load versus mid-span deflection, a) with and without shear reinforcement, b) various
694 layers of CFRP mesh in the top flange

695 **Fig. 16** a) *Ductal* behavior in tension, b) Load versus mid-span displacement for various tensile
696 behaviors

697 **Fig. 17** a) Positions of wheel loads investigated for the two span continuous configuration, b)
698 Ratio between applied and ultimate loads versus mid-span displacement

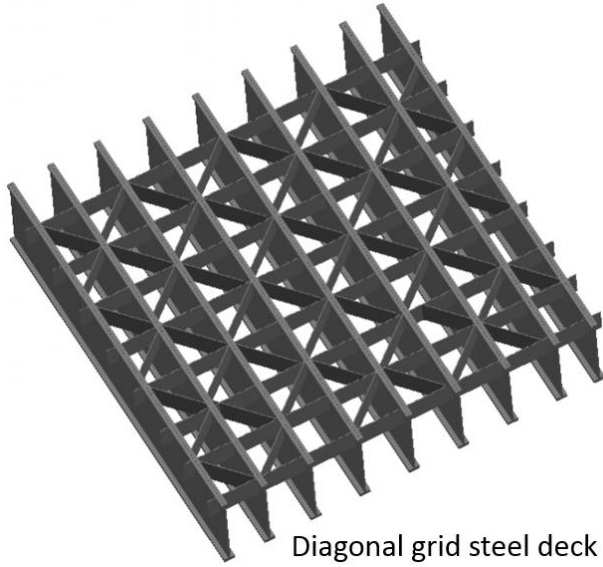
699 **Fig. 18** a) Most critical position of wheel loads for two span continuous case, b) Load versus
700 mid-span displacement for various layers of CFRP mesh in the top flange

701 **Fig. 19** Principal plastic tensile strains at failure for two span continuous configuration, a)
702 isometric view, b) top view

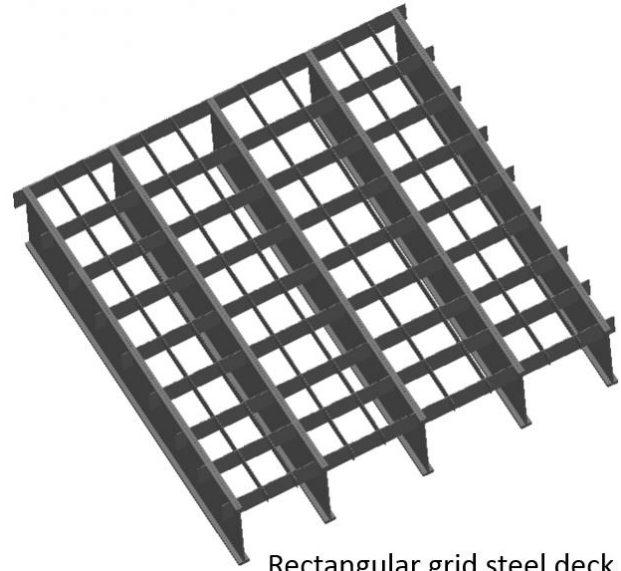
703 **Fig. 20** Performance at service

704

705

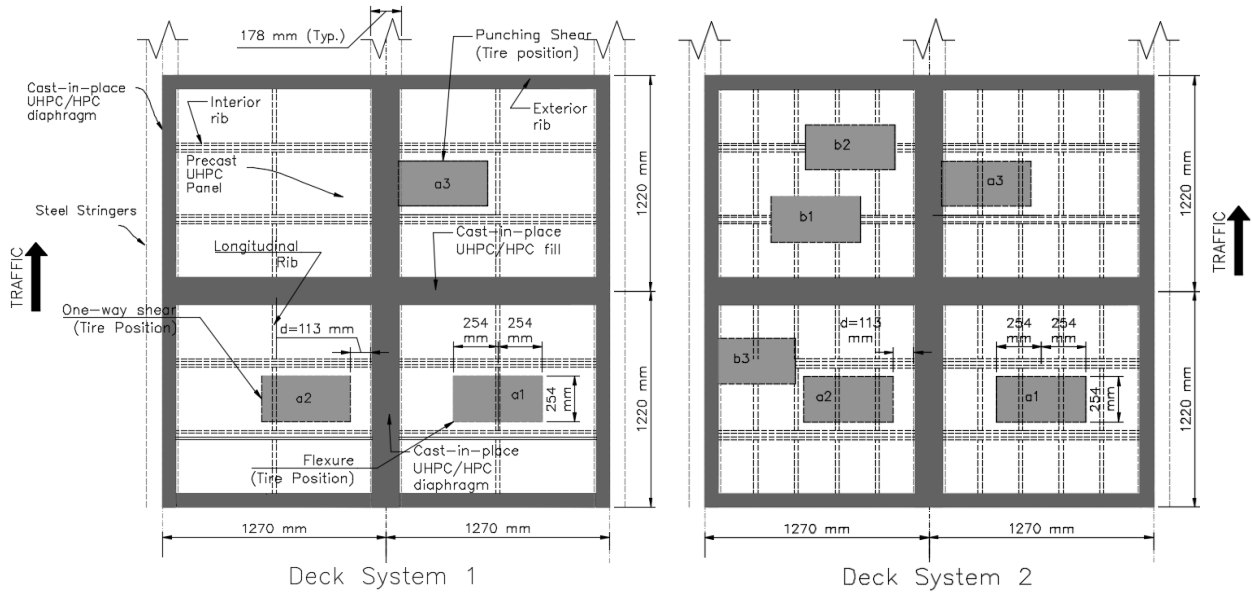


Diagonal grid steel deck



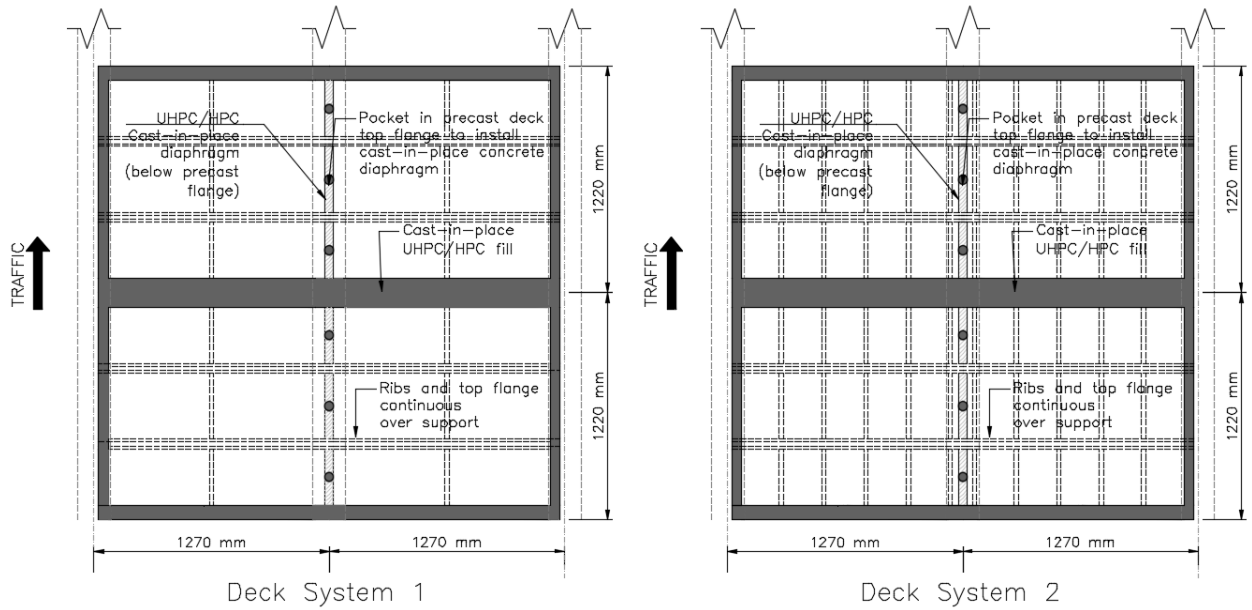
Rectangular grid steel deck

- 706
- 707
- 708
- 709
- 710
- 711
- 712
- 713
- 714
- 715
- 716
- 717
- 718
- 719
- 720
- 721
- 722
- 723
- 724



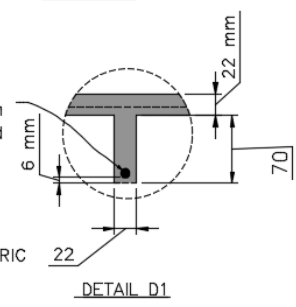
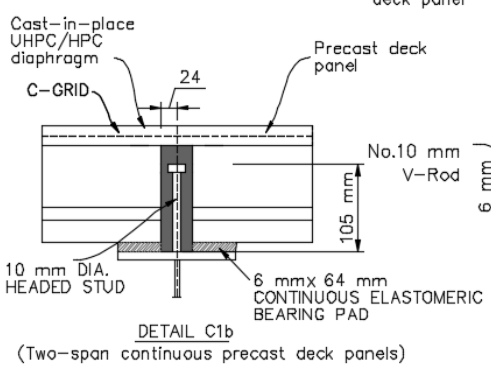
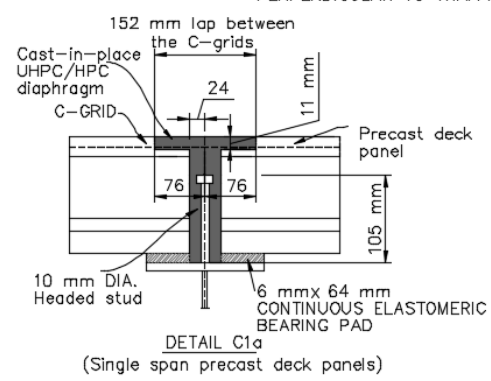
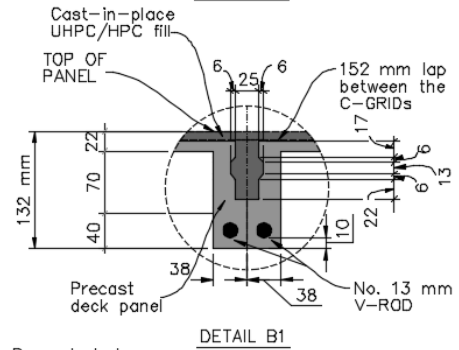
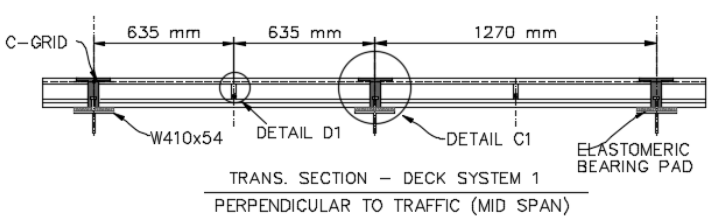
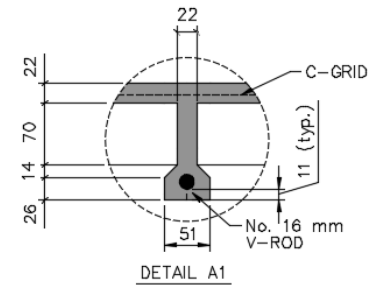
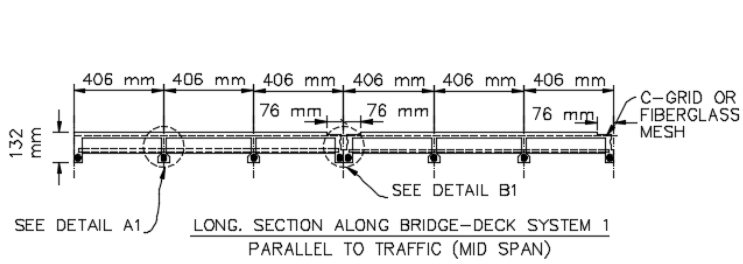
725
726

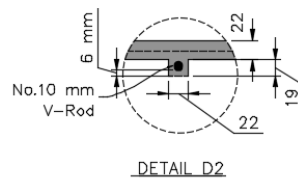
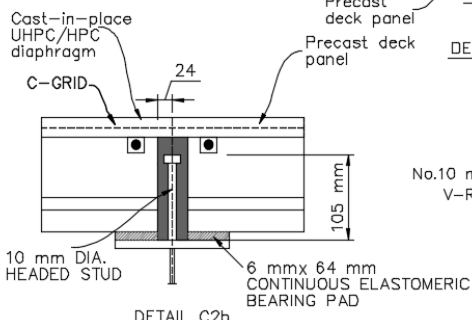
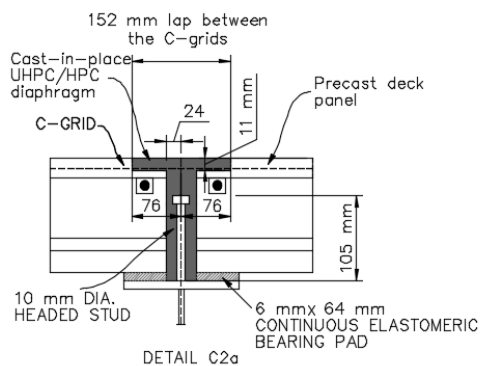
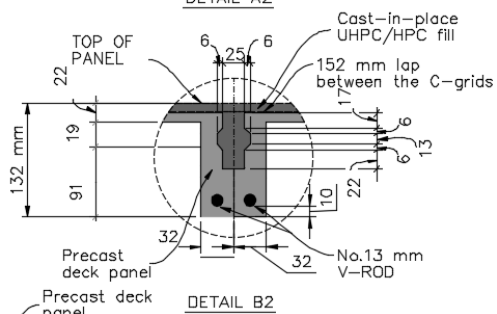
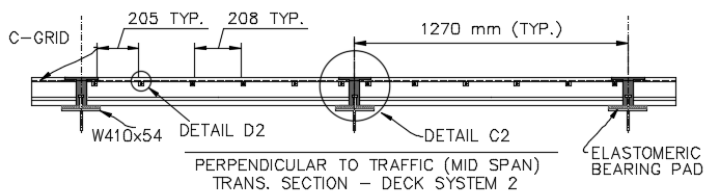
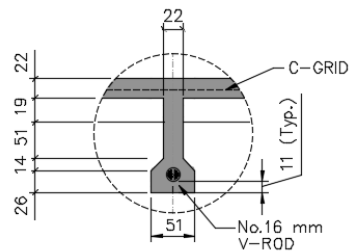
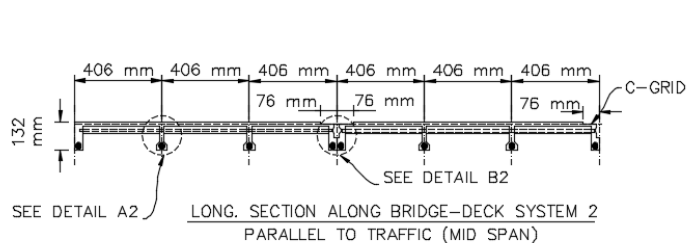
a) Single span precast deck panels



727
728
729
730

b) Two-span continuous precast deck panels

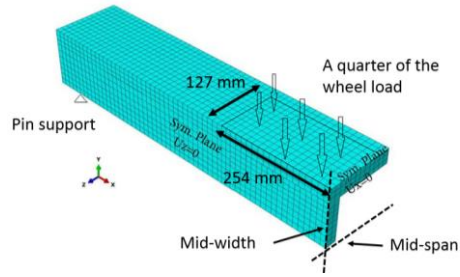




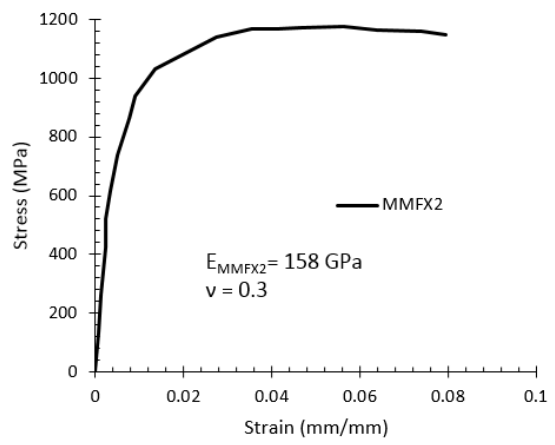
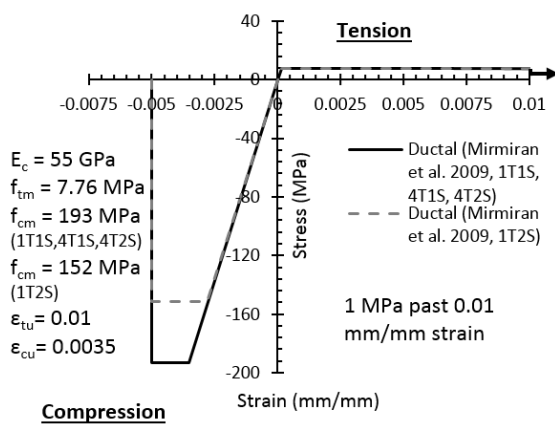
(Single span continuous precast deck panels)

(Two-span continuous precast deck panels)

- 732
- 733
- 734
- 735
- 736
- 737
- 738
- 739
- 740
- 741
- 742
- 743
- 744
- 745
- 746
- 747

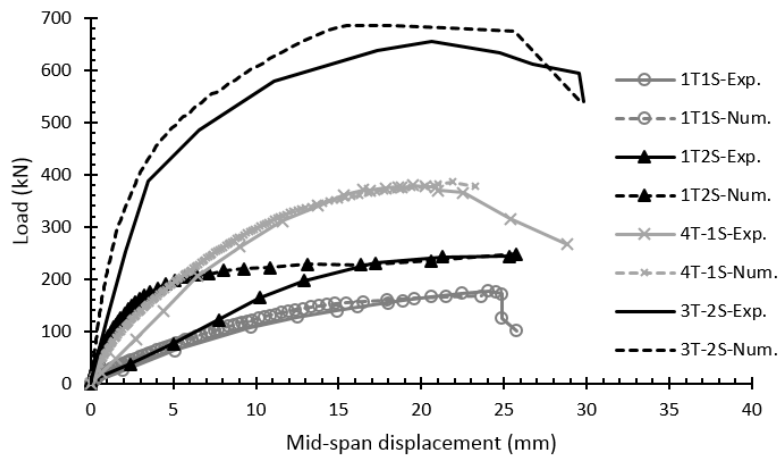


748
749
750
751
752
753
754
755
756
757
758
759
760
761
762
763
764
765
766
767
768
769
770
771
772



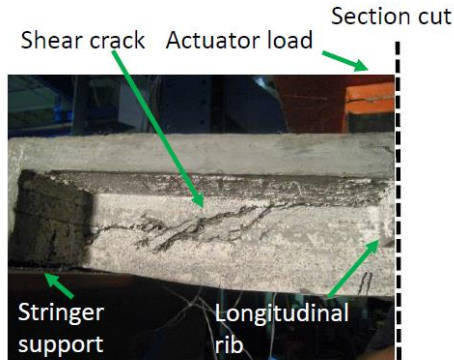
773
774
775
776

777
778
779
780
781
782
783
784
785
786
787
788
789
790
791
792
793
794
795

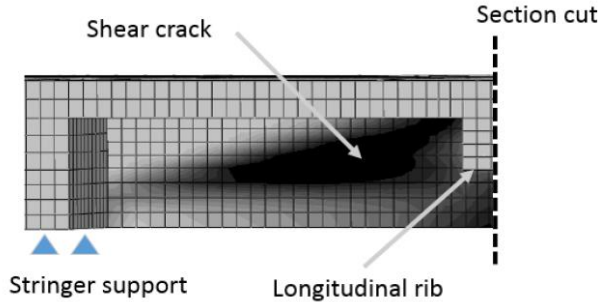
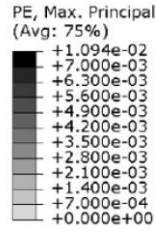


796
797
798
799
800
801
802
803
804
805
806
807
808
809
810
811

812
813
814

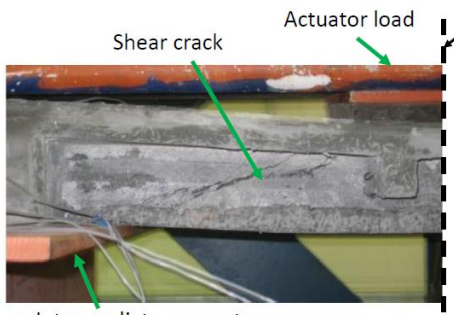


Experimental crack pattern (1T1S)
(Test performed by Mirmiran et al. (2009))

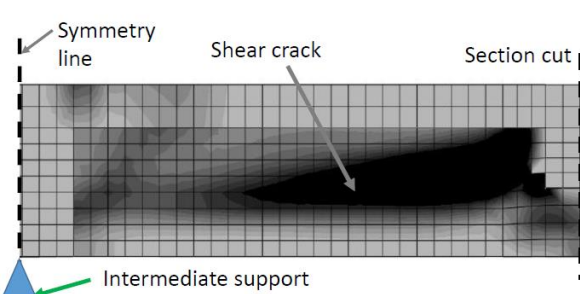
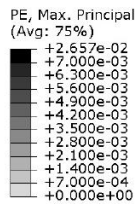


Simulated principle plastic tensile strain contours(1T1S)

815

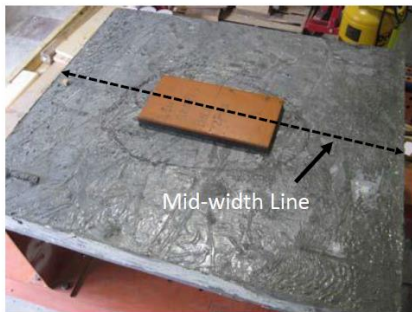


Experimental crack pattern (1T2S)
(Test performed by Mirmiran et al. (2009))

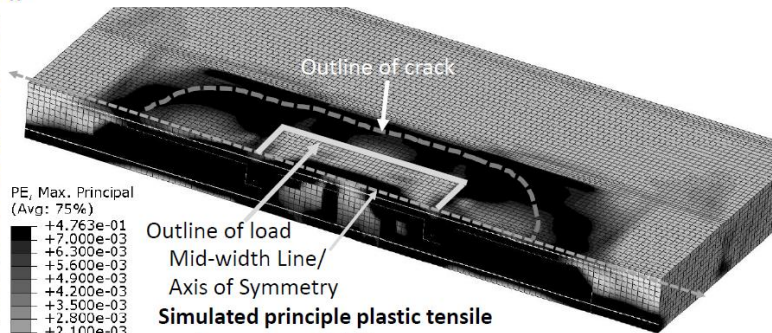
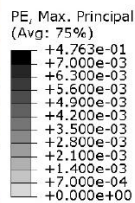


Simulated principle plastic tensile strain contours (1T2S)
(in black color: $\epsilon_{tu} \geq 0.0065$)

816

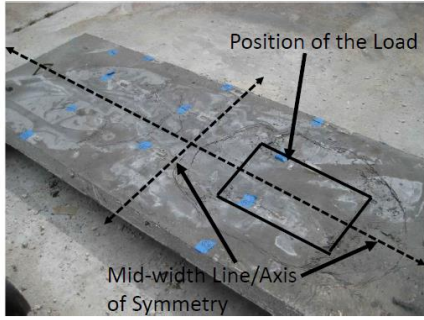


Experimental crack pattern (4T1S)
(Test performed by Mirmiran et al. (2009))

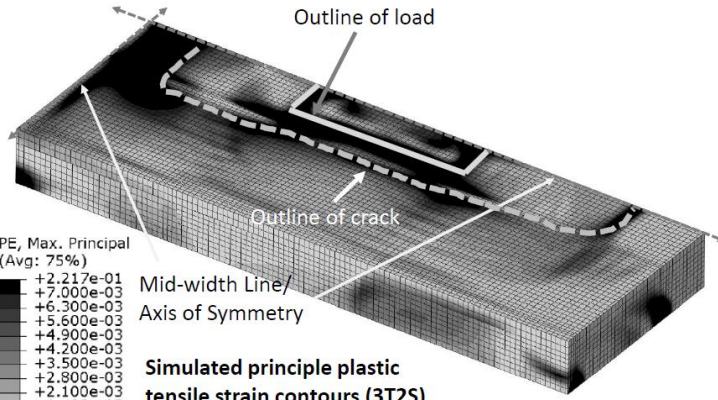


Simulated principle plastic tensile strain contours (4T1S)
(in black color: $\epsilon_{tu} \geq 0.0065$)

817



Experimental crack pattern (3T2S)
 (Test performed by Mirmiran et al. (2009))

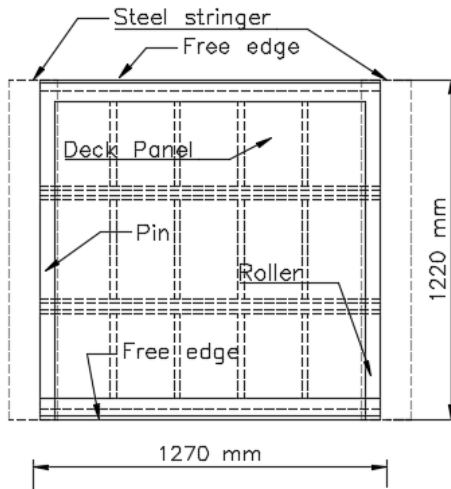


PE, Max. Principal
 (Avg: 75%)

+	2.217e-01
+	7.000e-03
+	6.300e-03
+	5.600e-03
+	4.900e-03
+	4.200e-03
+	3.500e-03
+	2.800e-03
+	2.100e-03
+	1.400e-03
+	7.000e-04
+	0.000e+00

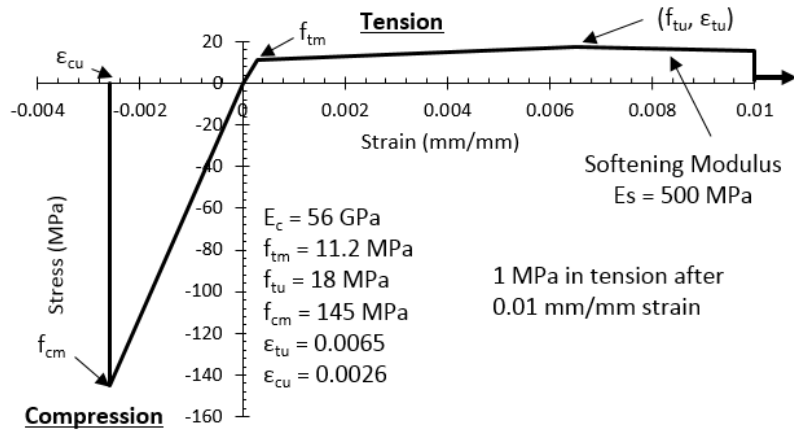
Simulated principle plastic tensile strain contours (3T2S)
 (in black color: $\epsilon_{tu} \geq 0.0065$)

818

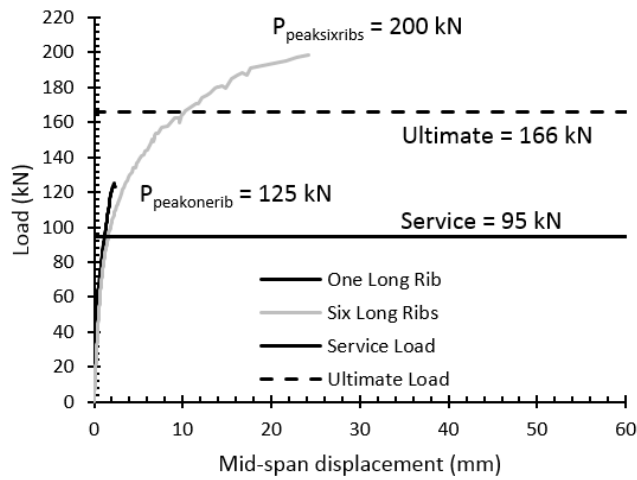
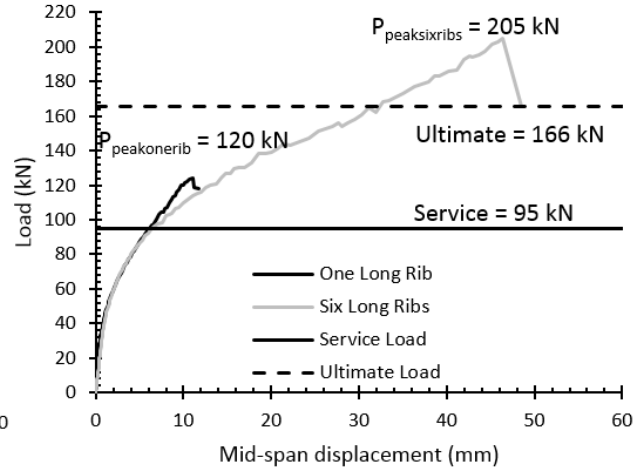
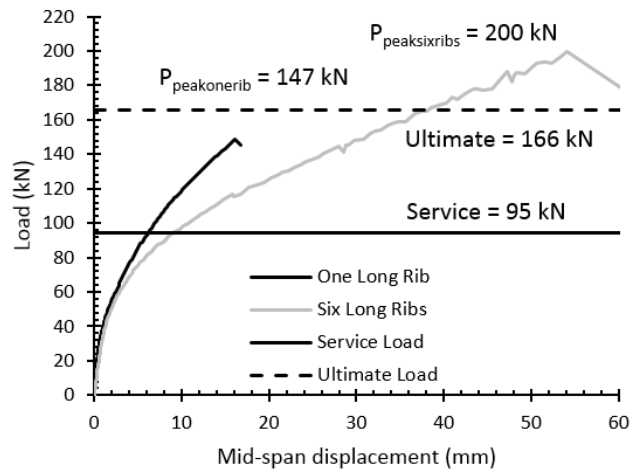


819
 820
 821
 822
 823
 824
 825
 826
 827
 828
 829
 830
 831
 832
 833
 834
 835
 836
 837
 838
 839
 840

841
842
843

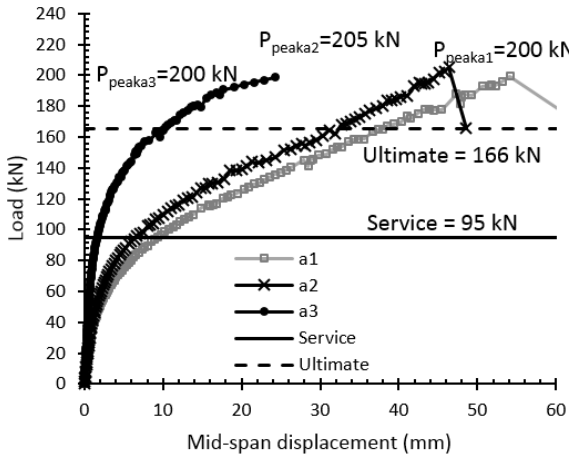


844
845
846
847
848
849
850
851
852
853
854
855
856
857
858
859
860
861
862
863
864
865
866

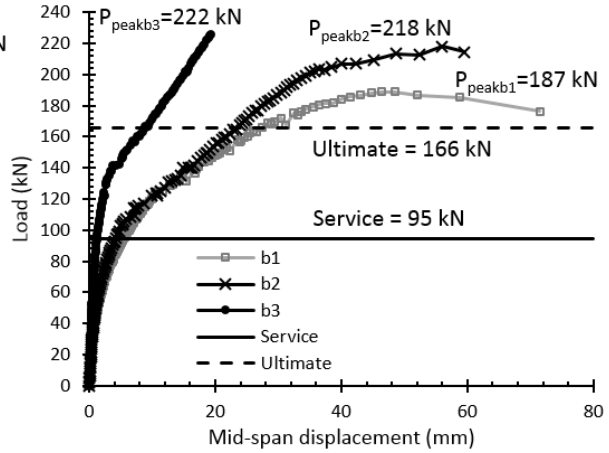


867
868

869
870
871
872
873
874
875
876
877

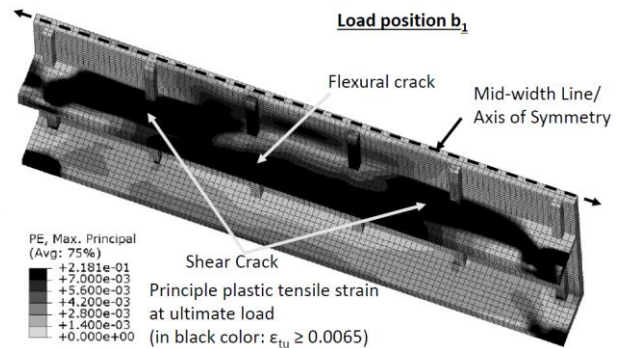
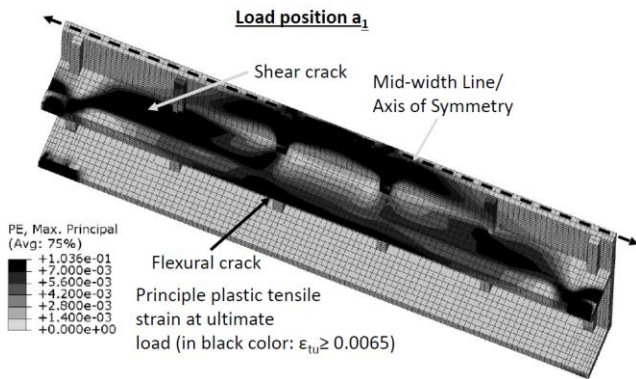


a)



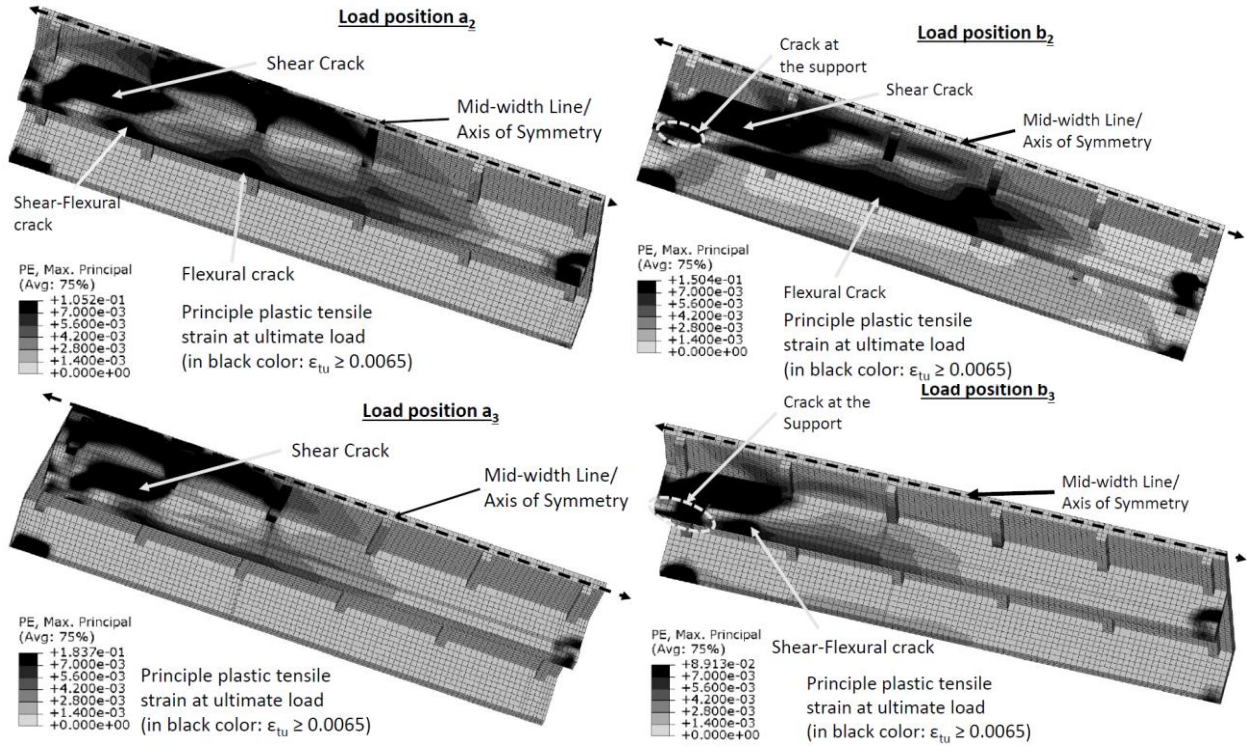
b)

878
879
880
881
882
883
884
885
886
887
888
889
890
891
892
893
894
895
896
897
898
899



900

901



902

903

904

905

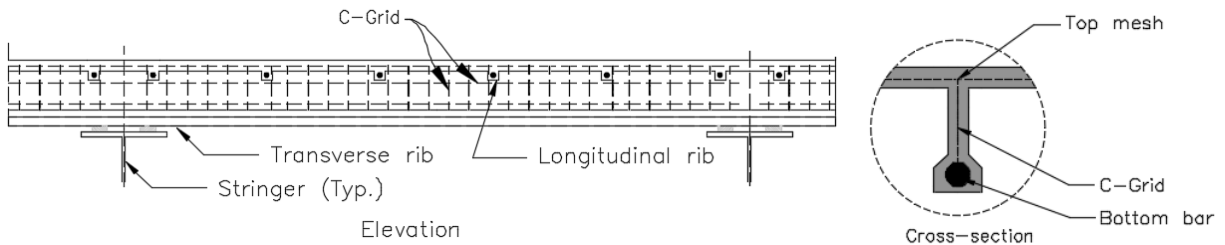
906

907

908

909

910



911

912

913

914

915

916

917

918

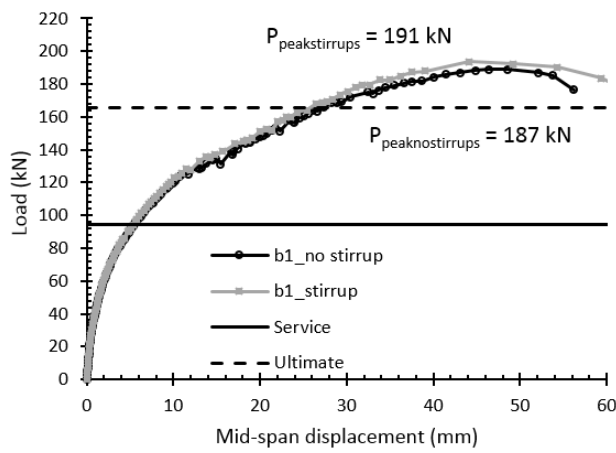
919

920

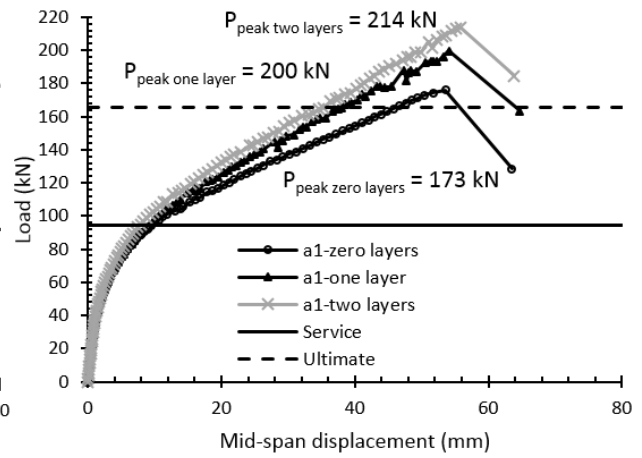
921

922

923
924
925
926
927
928
929
930
931
932
933
934
935

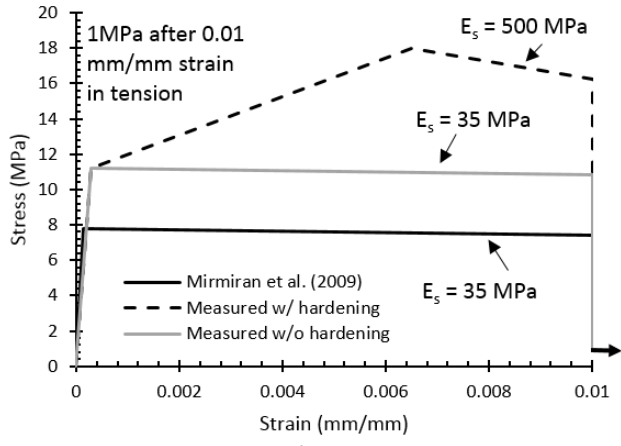


a)

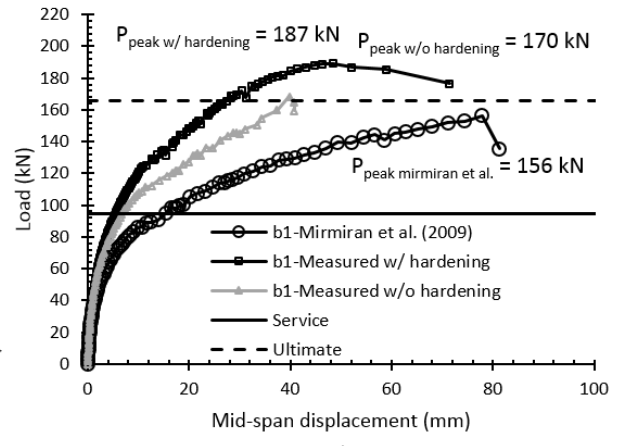


b)

936
937
938
939
940
941
942
943
944
945
946
947
948
949
950
951
952
953
954
955

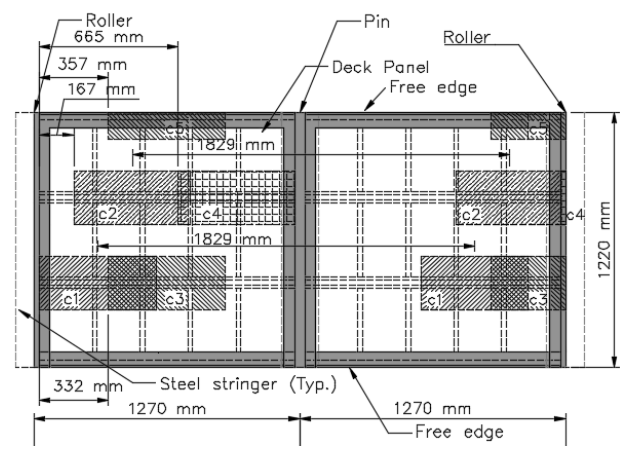


a)

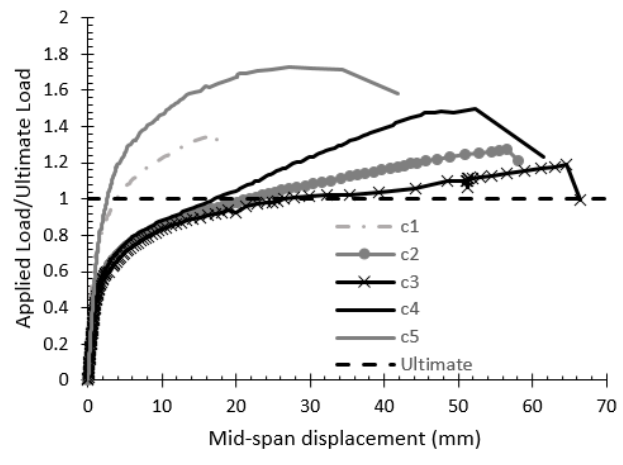


b)

956
 957
 958
 959
 960
 961
 962
 963
 964
 965
 966
 967
 968
 969
 970
 971
 972
 973
 974
 975
 976
 977
 978



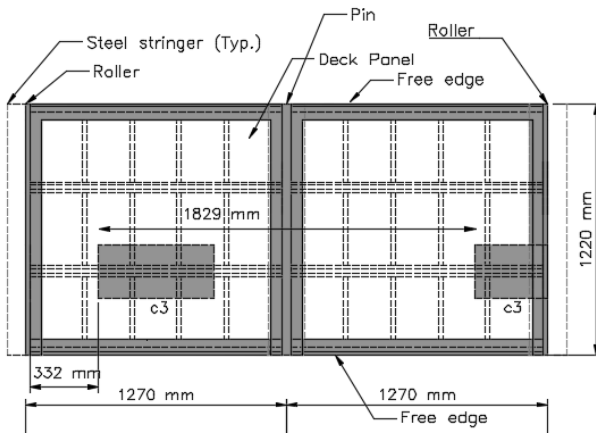
979



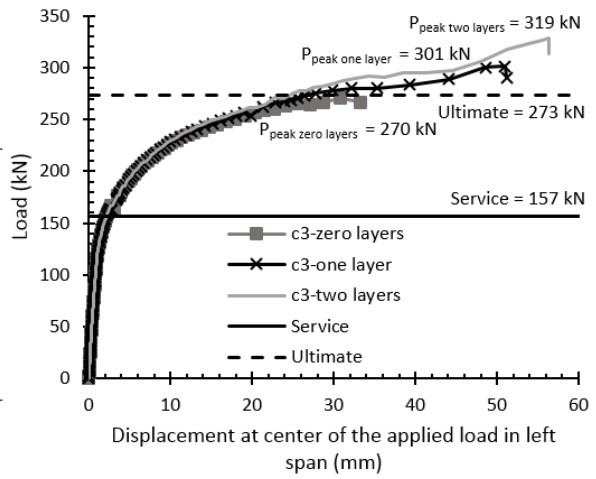
980
 981
 982
 983
 984
 985
 986
 987
 988
 989
 990
 991
 992
 993
 994
 995
 996
 997
 998
 999
 1000

a)

b)



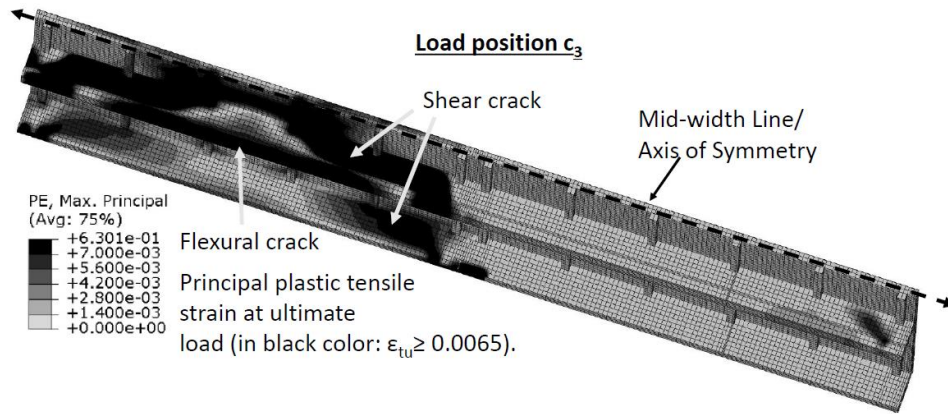
a)



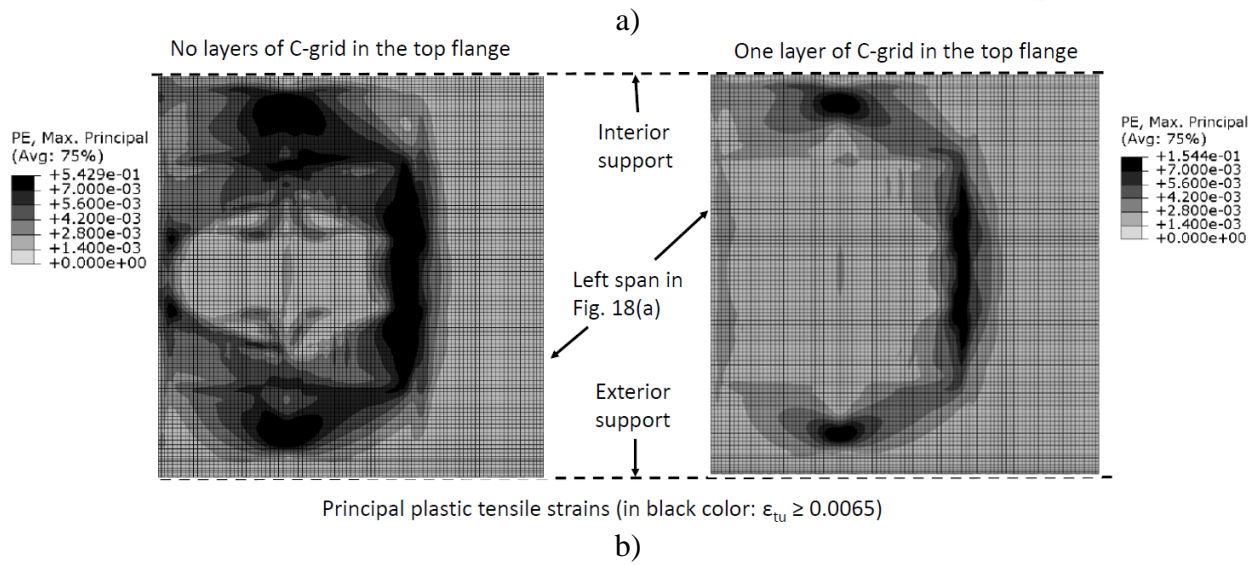
b)

1001
 1002
 1003
 1004
 1005
 1006
 1007
 1008
 1009
 1010
 1011
 1012
 1013

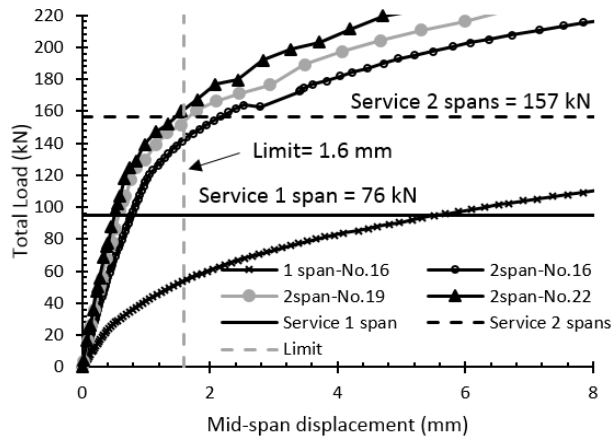
1014
1015
1016
1017
1018
1019
1020
1021
1022



1023
1024



1025
1026
1027
1028
1029
1030
1031
1032
1033
1034



1035
 1036
 1037
 1038

1039

Table 1 Recommendations for UHPC deck panel

Recommendations		Reason/Comment
Description	Value	
Panel Thickness (mm)	132	To be consistent with predominant existing grid deck thicknesses
Max. Panel weight (kN/m ²)	0.96	Calculated based on stringer reactions
Max. Span length (m)	1.27	It covers the majority of existing steel grid deck spans
Continuity	3+	Min. of three spans or simple span made continuous
Stringer	W410×54	Most common stringer

1040

1041

Table 2 Parameters for concrete damage plasticity model

Parameter	Value
Dilation angle (degrees)	45
Eccentricity	0.10
$\frac{\sigma_{bo}}{\sigma_{co}}$	1.77
K	0.67
Viscosity parameter	0

1042

1043

Table 3 Comparison of peak loads obtained numerically and experimentally

Specimen Description	Peak Loads (kN)		Ratio = P _{Num} /P _{Exp}
	Numerical	Experimental	
1T1S	168	182	0.92
1T2S	248	246	1.01
4T1S	387	377	1.03
3T2S	686	656	1.05

Average = 1.00
COV = 0.06

1044

1045

Table 4 Computed stress versus developable stress

Type	Size	Transverse			Longitudinal		
		f_{je} (MPa)	$f_{computed}$ (MPa)	$f_{je}/f_{computed}$	f_{je} (MPa)	$f_{computed}$ (MPa)	$f_{je}/f_{computed}$
GFRP	No.10				852	690	1.24
	No.13	1064	830	1.28			
	No.16	926	758	1.22			
	No.19	822	634	1.30			
	No. 22	750	482	1.55			

1046

1047